



# Synthesis and electrochemical property of $x\text{Li}_2\text{MnO}_3 \cdot (1-x)\text{LiMnO}_2$ composite cathode materials derived from partially reduced $\text{Li}_2\text{MnO}_3$



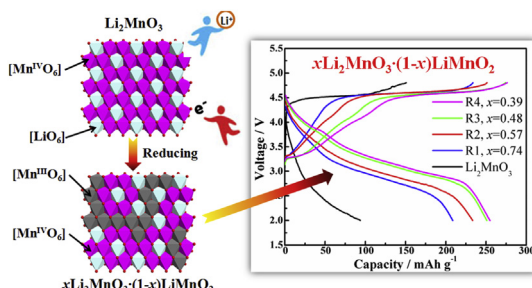
Qinggang Zhang, Tianyou Peng\*, Dan Zhan, Xiaohong Hu\*

College of Chemistry and Molecular Science, Wuhan University, Wuhan 430072, China

## HIGHLIGHTS

- $x\text{Li}_2\text{MnO}_3 \cdot (1-x)\text{LiMnO}_2$  composites are synthesized by partially reducing  $\text{Li}_2\text{MnO}_3$ .
- The layered structure with reduced Mn valance state is maintained.
- An initial charge/discharge profile similar to the Li-rich solid solutions.
- An improved rate performance with reversible capacity of  $>210 \text{ mAh g}^{-1}$  is obtained.

## GRAPHICAL ABSTRACT



## ARTICLE INFO

### Article history:

Received 17 July 2013

Received in revised form

30 October 2013

Accepted 30 October 2013

Available online 9 November 2013

### Keywords:

Composite cathode material  
Lithium manganese oxide  
Lithium stearate  
Electrochemical property

## ABSTRACT

$x\text{Li}_2\text{MnO}_3 \cdot (1-x)\text{LiMnO}_2$  ( $x = 0.39, 0.48, 0.57, 0.74$ ) composites with a layered structure of  $C2/m$  symmetry are firstly synthesized with the assistance of the pyrolysis of *in situ* formed lithium stearate, which can partially reduce the electrochemically inactive  $\text{Li}_2\text{MnO}_3$ . The obtained composites used as cathode material of Li-ion battery exhibit excellent electrochemical property such as high reversible capacity ( $>210 \text{ mAh g}^{-1}$ ) and good rate performance with an initial charge/discharge profile similar to the Li-rich solid solution materials in the range of 2.0–4.8 V. Among those obtained composites, 0.57 $\text{Li}_2\text{MnO}_3$ –0.43 $\text{LiMnO}_2$  has the best cyclic and rate performance, because it contains enough  $\text{LiMnO}_2$  to stabilize the structure of  $\text{LiMnO}_2$  and has a suitable average valence state of Mn to balance the reversible capacity and Jahn–Teller effect. The present findings indicate that the pyrolysis of *in situ* formed lithium stearate on  $\text{Li}_2\text{MnO}_3$  particle surfaces is a simple and effective way to obtain Mn-based layered Li-rich composite cathode materials of Li-ion battery with good cyclic and rate performance.

© 2013 Elsevier B.V. All rights reserved.

## 1. Introduction

In the past decades, some layered lithium transition metal oxides have been extensively investigated and used as cathode materials for Li-ion battery. Compared with the widely used layered Co- or Ni-based cathode materials, layered Mn-based ones have some advantages such as lower cost, less toxic and safer on overcharge, which are very important feature especially in the

commercial application [1]. As a basic layered Mn-based cathode material, the charged  $\text{LiMnO}_2$  has lower heat effect in contact with the commercial liquid electrolyte of Li-ion battery than the extensively applied  $\text{LiFePO}_4$ ,  $\text{LiMn}_2\text{O}_4$ ,  $\text{LiCoO}_2$  and  $\text{LiNiO}_2$ , and therefore the layered  $\text{LiMnO}_2$  as cathode material would be beneficial for improving the safety of Li-ion battery [2]. Usually,  $\text{LiMnO}_2$  has two kinds of crystal structures: orthorhombic  $\text{LiMnO}_2$  ( $o\text{-LiMnO}_2$ ) and monoclinic  $\text{LiMnO}_2$  ( $m\text{-LiMnO}_2$ ). Although both of the  $\text{LiMnO}_2$  crystal phases are electrochemically active with a theoretical capacity of  $\sim 285 \text{ mAh g}^{-1}$ , the  $o\text{-LiMnO}_2$  with  $Pmnm$  symmetry is more thermodynamically stable than the  $m\text{-LiMnO}_2$  with  $C2/m$  symmetry. As a result, the synthesis of  $m\text{-LiMnO}_2$  is relatively

\* Corresponding authors. Tel./fax: +86 27 6875 2237.

E-mail addresses: [tpeng@whu.edu.cn](mailto:tpeng@whu.edu.cn) (T. Peng), [xihu88@126.com](mailto:xihu88@126.com) (X. Hu).

difficult through a conventional solid-state reaction process, and therefore  $m$ -LiMnO<sub>2</sub> is usually fabricated by an ion-exchange process of layered NaMnO<sub>2</sub> [3]. Moreover, although it has been reported that doping with suitable ions can enhance the structural stability of  $m$ -LiMnO<sub>2</sub> cathode material to some extent [4–10], their reversible capacity is usually smaller than 200 mAh g<sup>-1</sup> with insufficient rate performance.

On the other hand, monoclinic Li<sub>2</sub>MnO<sub>3</sub> (Li[Li<sub>1/3</sub>Mn<sub>2/3</sub>]O<sub>2</sub>) with the same  $C2/m$  symmetry as  $m$ -LiMnO<sub>2</sub> has transition metal (TM) layers containing Mn<sup>4+</sup>/Li<sup>+</sup> molar ratio of 2:1 and a theoretical capacity up to 458 mAh g<sup>-1</sup> with respect to its initial mass of Li<sub>2</sub>MnO<sub>3</sub> [11,12]. Nevertheless, Li<sub>2</sub>MnO<sub>3</sub> is electrochemically inactive in the normal voltage range (<4.4 V vs. Li<sup>+</sup>/Li) of Li-ion battery because all Mn atoms in Li<sub>2</sub>MnO<sub>3</sub> are in +4 valence. Although Li<sub>2</sub>MnO<sub>3</sub> has a high theoretical capacity, it usually needs a high cut-off voltage (4.8 V vs. Li<sup>+</sup>/Li) during the initial charge process to activate Li<sub>2</sub>MnO<sub>3</sub>, and the capacity decay of the activated Li<sub>2</sub>MnO<sub>3</sub> is serious when cycling is performed at such high cut-off voltage. Therefore, Li<sub>2</sub>MnO<sub>3</sub> is usually integrated with layered LiMO<sub>2</sub> (M = Ni, Co or their mixture with Mn) or spinel LiM<sub>2</sub>O<sub>4</sub> (M = Ni, Mn or their mixture) to form Li-rich solid solution [12–16], which presented a specific capacity higher than 200 mAh g<sup>-1</sup>, and therefore are thought to be potential cathode materials of Li-ion battery [13–16]. However,  $x$ Li<sub>2</sub>MnO<sub>3</sub>·(1-x)Li<sub>1+y</sub>Mn<sub>2-y</sub>O<sub>4</sub> (0 < x < 1; 0 ≤ y ≤ 0.33) solid solution with layered–spinel mixed crystal phases but not  $x$ Li<sub>2</sub>MnO<sub>3</sub>·(1-x)LiMnO<sub>2</sub> solid solution with layered–layered monoclinic phase, is usually obtained from a conventional solid-state reaction method [16], and some other methods such as chemical lithiation (with LiI) or electrochemical insertion (initial discharge) of the acid leached Li<sub>2</sub>MnO<sub>3</sub> with a form as  $x$ Li<sub>2</sub>MnO<sub>3</sub>·(1-x)MnO<sub>2</sub>, are still not successful [17]. To the best of our knowledge,  $x$ Li<sub>2</sub>MnO<sub>3</sub>·(1-x)LiMnO<sub>2</sub> solid solution with layered–layered monoclinic phases has not been prepared up till now.

Herein, we developed a simple way with the assistance of the pyrolysis of *in situ* formed lithium stearate to synthesize  $x$ Li<sub>2</sub>MnO<sub>3</sub>·(1-x)LiMnO<sub>2</sub> solid solution by using monoclinic Li<sub>2</sub>MnO<sub>3</sub> as a host material. By this method, a series of composites  $x$ Li<sub>2</sub>MnO<sub>3</sub>·(1-x)LiMnO<sub>2</sub> (x = 0.39, 0.48, 0.57, 0.74) with layered–layered monoclinic phases were successfully prepared for the first time. These composites have a layered structure and an initial charge/discharge profile similar to the Li-rich solid solution materials. All obtained composites have a reversible capacity >210 mAh g<sup>-1</sup> and a significantly improved rate performance. The effects of the composite composition on the structure, cyclic stability and rate performance are also investigated.

## 2. Experimental

### 2.1. Preparation of Li<sub>2</sub>MnO<sub>3</sub> and $x$ Li<sub>2</sub>MnO<sub>3</sub>·(1-x)LiMnO<sub>2</sub>

Li<sub>2</sub>MnO<sub>3</sub> was synthesized by a conventional solid-state reaction process. Typically, MnCO<sub>3</sub> (Sinopharm Chemical Reagent, CP) and LiOH·H<sub>2</sub>O (Sinopharm Chemical Reagent, AR) mixture with a molar ratio of 1:2 was ball-milled for 12 h, and then calcined at 650 °C in air for 20 h to obtain Li<sub>2</sub>MnO<sub>3</sub>.

$x$ Li<sub>2</sub>MnO<sub>3</sub>·(1-x)LiMnO<sub>2</sub> composites were synthesized with the assistance of the pyrolysis of *in situ* formed lithium stearate by using monoclinic Li<sub>2</sub>MnO<sub>3</sub> as a host material. In a typical process, Li<sub>2</sub>MnO<sub>3</sub> (10 mmol) was mixed with stearic acid ethanol solution and stirred in water bath at 50 °C for 30 min. After centrifugation, the stearic acid treated Li<sub>2</sub>MnO<sub>3</sub> (SA-Li<sub>2</sub>MnO<sub>3</sub>) was dried in air. The resultant SA-Li<sub>2</sub>MnO<sub>3</sub> was put into a tube furnace and treated at 340 °C for 4 h under N<sub>2</sub> atmosphere. After cooling to room temperature, the product was washed with distilled water and dried

under vacuum at 120 °C overnight, and then re-calcined at 340 °C for 4 h under N<sub>2</sub> atmosphere for dehydration. Samples derived from the above process by adding 4.27, 4.98, 5.69 and 8.53 g stearic acid per mol Li<sub>2</sub>MnO<sub>3</sub> are labeled as R1, R2, R3 and R4, respectively. By measuring the mass of the stearic acid remained in the supernatant of the above centrifugation process, the adsorbed amount of stearic acid on Li<sub>2</sub>MnO<sub>3</sub> surfaces was determined to be 1.94, 2.22, 2.55, and 4.91 g per mol Li<sub>2</sub>MnO<sub>3</sub> for R1, R2, R3, and R4, respectively.

### 2.2. Materials characterization

Fourier transform infrared (FTIR) spectra of the precursors were measured by using an Avatar 330 FT-IR spectrometer. Chemical compositions of the products were analyzed by inductively coupled plasma atomic emission spectrometry (ICP-AES) and the carbon contents were evaluated by a VarioEL III elemental analyzer. The average valence state of Mn in the products was obtained by a titration method according to the previous report [18]. Typically, the sample was dissolved in H<sub>2</sub>SO<sub>4</sub> solution with excess Na<sub>2</sub>C<sub>2</sub>O<sub>4</sub> in 70 °C water bath, and then back-titrated by KMnO<sub>4</sub> standard solution. Total Mn content was titrated with EDTA standard solution at pH 6.00 by using xylene orange (XO) as indicator. The crystal and microstructure were characterized by a D8 Advance X-ray diffractometer with Cu K $\alpha$  radiation ( $\lambda$  = 0.15418 nm) between  $2\theta$  = 10 and 80° at a scan rate of 0.5° min<sup>-1</sup> and a JEM 2100 high resolution transmission electron microscope (HRTEM).

### 2.3. Electrochemical test

CR2016 coin-type cells were assembled in an Ar-filled glove box for the electrochemical measurements. The active materials, carbon black and PTFE with a weight ratio of 75:20:5 was mixed and pressed into a film followed by drying at 140 °C for 4 h. The film was cut into pieces with a size of 7 × 7 mm and pressed onto a stainless mesh as the cathode with electrode loading of ~5 mg. The anode was lithium foil and separated by a Celgard 2300 microporous membrane. The applied electrolyte is 1.0 M LiPF<sub>6</sub> solved in EC/DMC (1:1 in volume). The charging/discharging measurements were carried out on a battery cycler (LAND, China) by using the fabricated 2016 coin cells, and the electrochemistry impedance spectra (EIS) were recorded on a CHI 618C electrochemical workstation by using a three electrodes cell with active materials film as the cathode, lithium metal as both anode and reference electrodes. These EIS experiments are carried out over a frequency range from 10<sup>-2</sup> Hz to 10<sup>-5</sup> Hz with a sinusoidal excitation voltage of 10 mV, and EIS spectra are fitted by Z-view 2.0 software. Cyclic voltammogram (CV) tests were carried on a CHI 600C electrochemical workstation by using the above-mentioned three electrodes cells.

## 3. Results and discussion

### 3.1. Composition analyses of the composite materials

Fig. 1 shows the FTIR spectra of stearic acid, lithium stearate, SA-Li<sub>2</sub>MnO<sub>3</sub> and Li<sub>2</sub>MnO<sub>3</sub>. As can be seen, the pure stearic acid shows four characteristic absorption bands at about 1702, 1431, 1298 and 941 cm<sup>-1</sup>, which can be ascribable to the C=O vibration ( $\nu_{C=O}$ ), O–H bending ( $\delta_{O-H}$ ), C–O vibration coupling ( $\nu_{C-O}$ ) and O–H out-plane bending ( $\delta_{O-H, op}$ ) of –COOH of the stearic acid dimers [19–21], respectively. While the pure lithium stearate has four new absorption bands in the range of 1400–1600 cm<sup>-1</sup> rather than these characteristic absorption peaks of –COOH at about 1431 ( $\delta_{O-H}$ ) and 941 ( $\delta_{O-H, op}$ ) cm<sup>-1</sup>, and these new absorption bands can be ascribed to the asymmetric (1579, 1557 cm<sup>-1</sup>) and symmetric (1449, 1402 cm<sup>-1</sup>) stretching vibration of –COO<sup>-</sup> in lithium

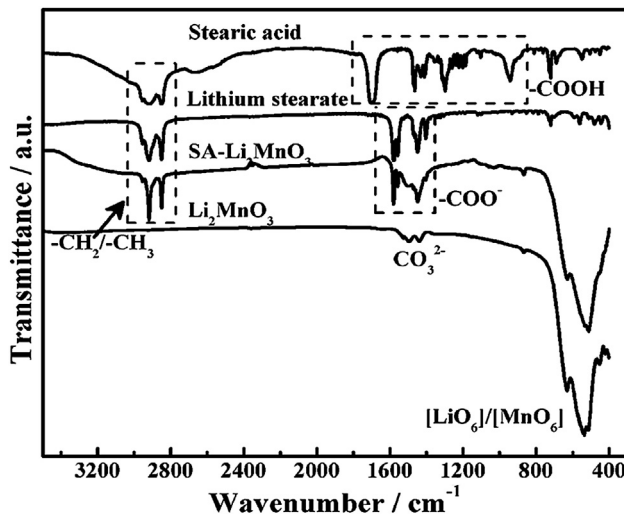


Fig. 1. FTIR spectra of stearic acid, lithium stearate, SA-Li<sub>2</sub>MnO<sub>3</sub> and Li<sub>2</sub>MnO<sub>3</sub>.

stearate [19]. Li<sub>2</sub>MnO<sub>3</sub> treated with stearic acid (SA-Li<sub>2</sub>MnO<sub>3</sub>) does not show the above-mentioned characteristic absorption peaks of –COOH at about 1431 and 941 cm<sup>−1</sup> attributable to O–H bending ( $\delta_{O-H}$ ) and O–H out-plane bending ( $\delta_{O-H, op}$ ), but it has four absorption bands in the range of 1400–1600 cm<sup>−1</sup>, which is very similar to the FTIR spectrum of lithium stearate.

The above results indicate that neither free stearic acid nor its H-bonded dimer exists in the resultant SA-Li<sub>2</sub>MnO<sub>3</sub>, implying that the Li<sup>+</sup> of Li<sub>2</sub>MnO<sub>3</sub> can replace the H<sup>+</sup> of –COOH to chemically bond with –COO<sup>−</sup> during the present stearic acid treating process of Li<sub>2</sub>MnO<sub>3</sub>. Namely, stearic acid is chemically adsorbed on Li<sub>2</sub>MnO<sub>3</sub> particles, and leading to the *in situ* formation of lithium stearate in the present process [20,21], which can be pyrolyzed at 340 °C under N<sub>2</sub> atmosphere and partially reduce the electrochemically inactive Li<sub>2</sub>MnO<sub>3</sub>. As can be seen from the element content and Mn valence state analytical results of these products listed in Table 1, the pristine Li<sub>2</sub>MnO<sub>3</sub> shows a Li/Mn molar ratio of 2.00 with an average Mn valence state of +4.01, which is very similar to the corresponding theoretical values, while product R1, R2, R3 and R4 show a Li/Mn molar ratio of 1.74, 1.57, 1.48 and 1.39 with an average Mn valence state of +3.75, +3.58, +3.48 and +3.37, respectively. Therefore, it can be concluded that the present pyrolysis process of *in situ* formed lithium stearate at 340 °C can lead to partial reduction of the electrochemically inactive Li<sub>2</sub>MnO<sub>3</sub>.

### 3.2. Microstructure analyses of the composite materials

Fig. 2 depicts the XRD patterns of the obtained Li<sub>2</sub>MnO<sub>3</sub> and composites. The pristine Li<sub>2</sub>MnO<sub>3</sub> shows a diffraction pattern corresponding to the monoclinic Li<sub>2</sub>MnO<sub>3</sub> (*m*-Li<sub>2</sub>MnO<sub>3</sub>) with a C2/m space group (PDF No.: 84-1634), while those partially reduced composites derived from the pyrolysis of SA-Li<sub>2</sub>MnO<sub>3</sub> at 340 °C still

show the main characteristic peaks of *m*-Li<sub>2</sub>MnO<sub>3</sub>, indicating the layered structure of Li<sub>2</sub>MnO<sub>3</sub> is preserved. According to the PDF cards shown in Fig. 2a, *m*-Li<sub>2</sub>MnO<sub>3</sub> and *m*-LiMnO<sub>2</sub> have very similar crystal structures with C2/m symmetry, and the reflection peak at  $2\theta = 18\text{--}19^\circ$  is related to the reflection of (001) planes of C2/m space group, and the corresponding *d*-spacing for *m*-Li<sub>2</sub>MnO<sub>3</sub> and *m*-LiMnO<sub>2</sub> is 0.4743 and 0.4842 nm. According to the element contents and Mn valence states of those composites shown in Table 1, the product R1, R2, R3 and R4 can be written as a form of  $x\text{Li}_2\text{MnO}_3 \cdot (1-x)\text{LiMnO}_2$  ( $x = 0.74, 0.57, 0.48, 0.39$ ). Moreover, the (001) diffraction peak of those  $x\text{Li}_2\text{MnO}_3 \cdot (1-x)\text{LiMnO}_2$  slightly shifts to lower  $2\theta$  (Fig. 2a) with the full width at half maximum (FWHM) widened from 0.51° (for Li<sub>2</sub>MnO<sub>3</sub>) to 0.58° (for R4), and hence the *d*-spacing is extended from 0.4741 to 0.4764 nm (Table 1) with decreasing the *x* value from 1.00 to 0.39, which means the increasing molar ratio of *m*-LiMnO<sub>2</sub> in the composite. Meanwhile, the other main diffraction peaks of Li<sub>2</sub>MnO<sub>3</sub> are also broadened with enhancing the *m*-LiMnO<sub>2</sub> content in the composite as shown in Fig. 2a.

The above results seem to indicate that a solid solution of Li<sub>2</sub>MnO<sub>3</sub> and LiMnO<sub>2</sub> can be formed during the present preparation processes. Because if Li<sub>2</sub>MnO<sub>3</sub> and LiMnO<sub>2</sub> are not solved, the (001) diffraction peak of *m*-LiMnO<sub>2</sub> at least in product R4 with LiMnO<sub>2</sub> content up to ~61% should separate from the (001) diffraction peak (at the red (in the web version) vertical dash line in Fig. 2a) of Li<sub>2</sub>MnO<sub>3</sub>, and can be observed clearly at  $2\theta = 18.31^\circ$  (at the blue vertical solid line in Fig. 2a). However, there is only a single peak between the blue and red line for those partially reduced products. On the other hand, those weak diffraction peaks located at  $2\theta = 20\text{--}25^\circ$  for the pristine Li<sub>2</sub>MnO<sub>3</sub> are related to the superstructure due to the Li/Mn ordering in the TM layers, and contributed by the reflections of (020), (110) and (−111) planes [12], while *m*-LiMnO<sub>2</sub> has no such superstructure peaks because there is no Li ion existing in the TM layers (ref. Fig. 2b and c) though *m*-LiMnO<sub>2</sub> has the same symmetry as the *m*-Li<sub>2</sub>MnO<sub>3</sub>. Moreover, all of those composites have the superstructure diffraction peak at  $2\theta = 20\text{--}25^\circ$ , which is a diffraction feature of  $x\text{Li}_2\text{MnO}_3 \cdot (1-x)\text{LiMO}_2$  (M = Mn, Ni, Co), especially when Li<sub>2</sub>MnO<sub>3</sub> ratio is in a high level [14,15]. Those peak intensities related to the superstructure are weakening upon enhancing *m*-LiMnO<sub>2</sub> content, indicating the decrease of the Li content in the TM layers of those composites. Once *x* = 0.39, the composite shows some new diffraction peaks attributable to (−202) and (−113)/(−311) reflections of *m*-LiMnO<sub>2</sub> (PDF No.: 87-1255) in addition to that of *m*-Li<sub>2</sub>MnO<sub>3</sub>, indicating the existence of some *m*-LiMnO<sub>2</sub>-like regions in those composites. As a result, it can be concluded that the present pyrolysis process of *in situ* formed lithium stearate on Li<sub>2</sub>MnO<sub>3</sub> can lead to the formation of  $x\text{Li}_2\text{MnO}_3 \cdot (1-x)\text{LiMnO}_2$  solid solution with layered–layered monoclinic phase.

The pristine Li<sub>2</sub>MnO<sub>3</sub>, R1 and R4 are chosen to further investigate the detailed structure evolution during the pyrolysis process of *in situ* formed lithium stearate on Li<sub>2</sub>MnO<sub>3</sub> particles. TEM images (Fig. 3a–c) indicate that the morphology and particle size of the Li<sub>2</sub>MnO<sub>3</sub> nanoparticles are altered during the pyrolysis process, and

**Table 1**  
The experimental results of Li/Mn atom ratio, carbon (C) content, Mn average valence and the corresponding calculated values of *x* and *d*<sub>001</sub>-spacing of  $x\text{Li}_2\text{MnO}_3 \cdot (1-x)\text{LiMnO}_2$ .

	Li/Mn <sub>exp.</sub>	C <sub>exp/</sub> wt%	Mn valance <sub>exp.</sub>	<i>x</i> <sub>cal.</sub>	$x\text{Li}_2\text{MnO}_3 \cdot (1-x)\text{LiMnO}_2$	<i>d</i> <sub>001/nm</sub>
Li <sub>2</sub> MnO <sub>3</sub>	2.00	0	+4.01	1.00		0.4741
R1	1.74	1.71	+3.75	0.74	0.74Li <sub>2</sub> MnO <sub>3</sub> · 0.26LiMnO <sub>2</sub>	0.4746
R2	1.57	2.67	+3.58	0.57	0.57Li <sub>2</sub> MnO <sub>3</sub> · 0.43LiMnO <sub>2</sub>	0.4754
R3	1.48	2.88	+3.48	0.48	0.48Li <sub>2</sub> MnO <sub>3</sub> · 0.52LiMnO <sub>2</sub>	0.4759
R4	1.39	4.11	+3.37	0.39	0.39Li <sub>2</sub> MnO <sub>3</sub> · 0.61LiMnO <sub>2</sub>	0.4764

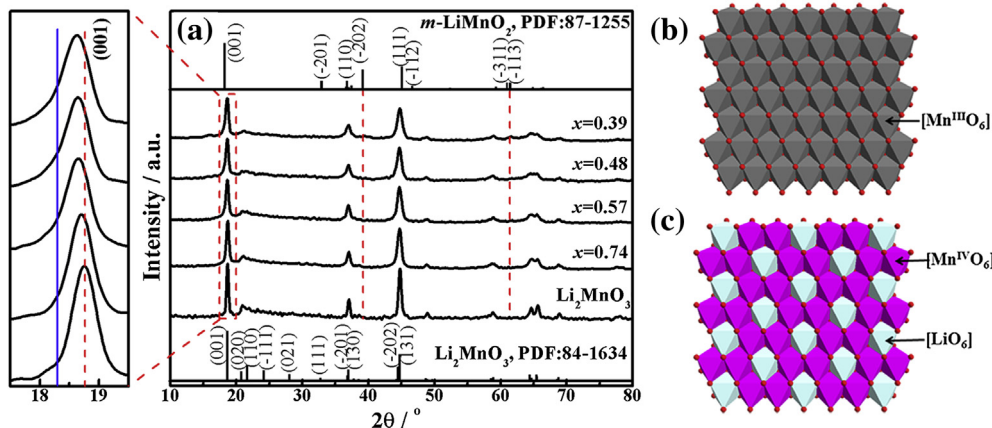


**Fig. 2.** XRD patterns (a) of  $\text{Li}_2\text{MnO}_3$  and  $x\text{Li}_2\text{MnO}_3 \cdot (1-x)\text{LiMnO}_2$  ( $x = 0.39, 0.48, 0.57, 0.74$ ); and the schematic drawings of the TM layer structures in  $m\text{-LiMnO}_2$  (b) and  $\text{Li}_2\text{MnO}_3$  (c).

the obtained  $x\text{Li}_2\text{MnO}_3 \cdot (1-x)\text{LiMnO}_2$  products show smaller particles with much more coarse surfaces than the pristine one. HRTEM images (Fig. 3d–f) show that all of  $\text{Li}_2\text{MnO}_3$ , R1 and R4 have clear parallel lattice fringes that can be ascribed to the (001) planes of the  $C2/m$  layered structure. The interlayer spacing of  $\text{Li}_2\text{MnO}_3$ , R1 and R4 slightly expands from 0.474 to 0.476 nm, which is consistent with the above XRD results shown in Table 1. Moreover, some stack faults can be observed in the HRTEM image of R4, but it is scarcely observed from the HRTEM images of  $\text{Li}_2\text{MnO}_3$  or R1, and therefore it can be conjectured that those stack faults may be associated with the interlayer spacing gap of  $\text{LiMnO}_2$  and  $\text{Li}_2\text{MnO}_3$ . Since the  $\text{LiMnO}_2$  content in R4 is the highest one (~61%) among those composites, and therefore its gap accumulation and stack faults are more obvious than the other samples. In fact, the interlayer spacing of the left (0.484 nm) and right (0.474 nm) side of the stack fault (Fig. 3f) can be ascribed to the (001) planes of  $m\text{-LiMnO}_2$  and  $m\text{-Li}_2\text{MnO}_3$ , respectively. It suggests the coexistence of  $m\text{-LiMnO}_2$ / $\text{Li}_2\text{MnO}_3$ -like region in the product. Similarly, the spinel domains

were also observed from the HRTEM image of a layer–spinel composite [16]. Based on the above results and discussion, it can be concluded that  $\text{Li}_2\text{MnO}_3$  and  $m\text{-LiMnO}_2$  in  $x\text{Li}_2\text{MnO}_3 \cdot (1-x)\text{LiMnO}_2$  are solved well especially for those composites with low  $\text{LiMnO}_2$  content (with high  $x$  values), while  $m\text{-LiMnO}_2$  domains would appear accompanied by the formation of stack faults and decrease of crystallinity in the composite with low  $x$  value.

### 3.3. Electrochemical properties of the composite materials

Fig. 4 shows the initial charge/discharge profiles, cyclic performance and the corresponding columbic efficiency of  $\text{Li}_2\text{MnO}_3$  and  $x\text{Li}_2\text{MnO}_3 \cdot (1-x)\text{LiMnO}_2$  ( $x = 0.39, 0.48, 0.57, 0.74$ ) at a current density of 30 mA g<sup>-1</sup>. As can be seen from Fig. 4a, the initial charge/discharge profiles of the  $\text{Li}_2\text{MnO}_3$  electrode at a 4.8 V cut-off voltage are similar to the previous reports [22,23]. Nevertheless, the present  $\text{Li}_2\text{MnO}_3$  exhibits smaller charge/discharge capacity (150/94 mA g<sup>-1</sup>) than the reported values [22,23]. It can be ascribed to

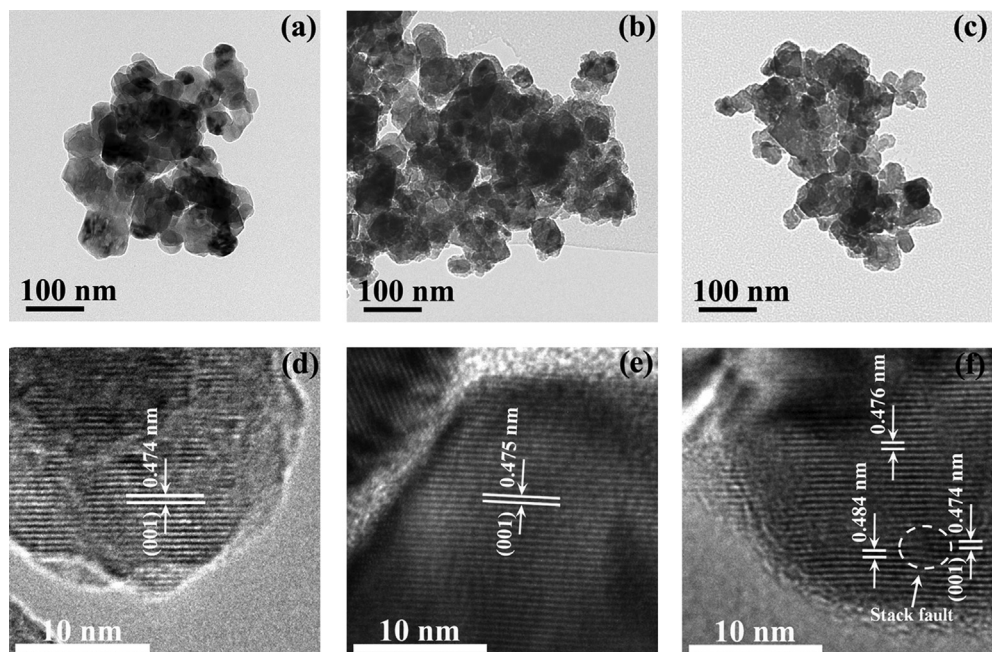


**Fig. 3.** TEM and HRTEM images of the obtained  $\text{Li}_2\text{MnO}_3$  (a, d), R1 (b, e) and R4 (c, f).

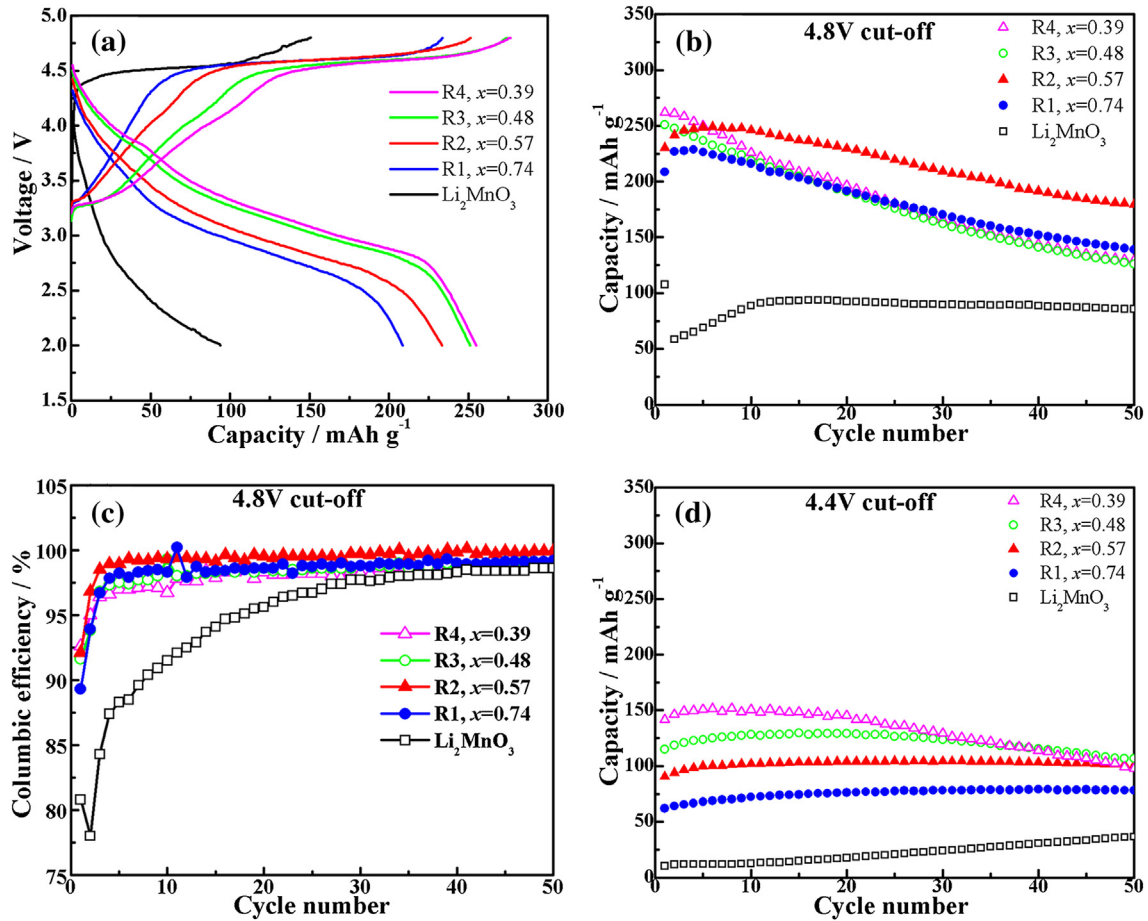


**Fig. 4.** Initial charge/discharge profiles (a), cyclic performances (b) and its corresponding columbic efficiency (c) of  $\text{Li}_2\text{MnO}_3$  and  $x\text{Li}_2\text{MnO}_3 \cdot (1-x)\text{LiMnO}_2$  ( $x = 0.39, 0.48, 0.57, 0.74$ ) at a current density of  $30 \text{ mA g}^{-1}$  under  $4.8 \text{ V}$  cut-off voltage. For comparison, the cyclic performances of the above samples under  $4.4 \text{ V}$  cut-off voltage are also depicted in (d).

the present lower testing temperature ( $25 \text{ }^\circ\text{C}$ ) than that ( $55 \text{ }^\circ\text{C}$ ) of these reports with higher capacity [22]. However, the profile shape of  $x\text{Li}_2\text{MnO}_3 \cdot (1-x)\text{LiMnO}_2$  is different from that of  $\text{Li}_2\text{MnO}_3$  but quite similar to the Li-rich cathode materials [12,13,15,24], which has a slop below  $4.4 \text{ V}$  and a voltage plateau at  $\sim 4.5 \text{ V}$ . This slop is associated to the solid-state redox reaction in  $\text{LiMO}_2$ , and the charge plateau at  $\sim 4.5 \text{ V}$  is related to simultaneously extraction of Li and O atoms from particles [24]. As for the present  $x\text{Li}_2\text{MnO}_3 \cdot (1-x)\text{LiMnO}_2$ , the above solid-state reaction is  $\text{Li}^+$  extraction and  $\text{Mn}^{3+}$  oxidation in the layered  $\text{LiMnO}_2$ . As shown in Fig. 4a, the more the  $\text{LiMnO}_2$  content is, the longer this slop. Meanwhile, it should be noted that the first discharge capacities ( $>210 \text{ mAh g}^{-1}$ ) of all  $x\text{Li}_2\text{MnO}_3 \cdot (1-x)\text{LiMnO}_2$  are much larger than that of the  $\text{Li}_2\text{MnO}_3$  and increase upon enhancing the  $\text{LiMnO}_2$  content, and the product R4 with a form of  $0.39\text{Li}_2\text{MnO}_3 \cdot 0.61\text{LiMnO}_2$  has the largest initial discharge capacity ( $255 \text{ mAh g}^{-1}$ ), corresponding to an energy density of  $849 \text{ Wh kg}^{-1}$  with an average voltage of  $3.33 \text{ V}$ . Moreover, the first cycle columbic efficiencies ( $>90\%$ ) of those  $x\text{Li}_2\text{MnO}_3 \cdot (1-x)\text{LiMnO}_2$  composites are also higher than that (83.2%) of the pristine  $\text{Li}_2\text{MnO}_3$  and the Li-rich cathode material without acid-treating [13].

Although the initial discharge capacity of those composites at  $4.8 \text{ V}$  cut-off voltage is increasing upon enhancing the  $\text{LiMnO}_2$  content, their capacity decays are more obvious than the pristine  $\text{Li}_2\text{MnO}_3$  as shown in Fig. 4b. It is interesting that the discharge capacities of R1 and R2 with  $x > 0.5$  are increasing in the first several cycles under  $4.8 \text{ V}$  cut-off voltage, and R2 shows the best cyclic performance in the following cycles among those

composites. On the other hand, the columbic efficiency of the first cycle is increasing from 83.2% to  $\sim 92.5\%$  as the  $x$  value decreasing from 1.00 to 0.57 as can be seen from Fig. 4c. During the following several cycles, the columbic efficiencies of all composites are quickly increasing while the pristine  $\text{Li}_2\text{MnO}_3$  shows much slower increasing speed. After 5 cycles, the columbic efficiency is almost steady and R2 has the highest value ( $\sim 99.5\%$ ), indicating R2 has the best cyclic stability among those samples. A similar conclusion can be obtained by comparing the cyclic performances of those composites under different cut-off voltage ( $4.4$  and  $4.8 \text{ V}$ ) as shown in Fig. 4b and d. As can be seen, the discharge capacities of those composites under  $4.4 \text{ V}$  cut-off voltage are much lower than that under  $4.8 \text{ V}$  cut-off voltage. Also, the discharge capacities of those composites under  $4.4 \text{ V}$  cut-off voltage are increasing as decreasing  $x$  value, but those composites with lower  $x$  value (for example R3 and R4) show much more obvious capacity fading than that with higher  $x$  value (for example R1 and R2) as can be observed from Fig. 4d, and therefore, R2 also has the best cyclic performance under  $4.4 \text{ V}$  cut-off voltage among these composites.

As can be seen from the charge/discharge profiles of the 2nd, 5th, 10th, 20th and 50th cycle shown in Fig. 5a, the capacity decay is mainly attributed to the significant shortening of the discharge plateau at  $\sim 3.0 \text{ V}$ . As for a pure  $\text{LiMnO}_2$ , this phenomenon is common, which is associated to Mn dissolution stemmed from the Jahn–Teller distortion [25]. It is known that when the average Mn oxidation state is lower than  $+3.5$ , the Jahn–Teller distortion would result in the disproportionation of  $\text{Mn}^{3+}$  to  $\text{Mn}^{4+}$  and  $\text{Mn}^{2+}$ . Induced by the acids generated from electrolyte decomposition,

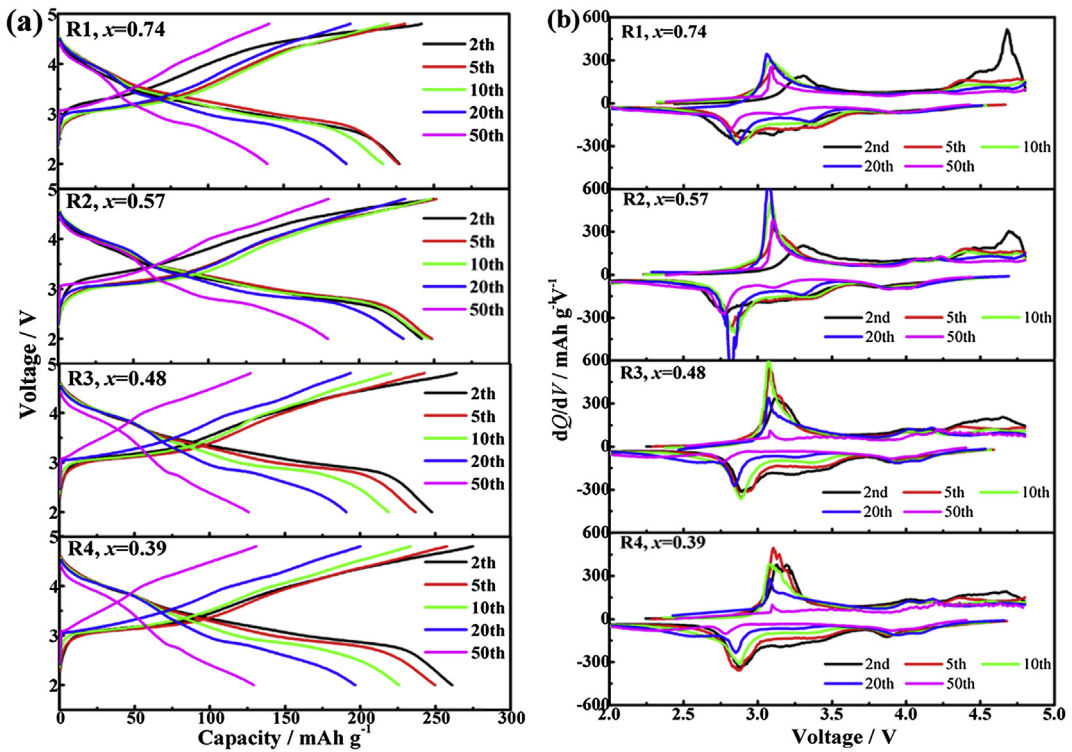


Fig. 5. The 2nd, 5th, 10th, 20th and 50th cycle charge/discharge profiles (a) and their corresponding  $dQ/dV$  plots (b) of  $x\text{Li}_2\text{MnO}_3 \cdot (1-x)\text{LiMnO}_2$  ( $x = 0.39, 0.48, 0.57, 0.74$ ).

$\text{Mn}^{2+}$  can easily dissolve in the electrolyte, and then resulting in active mass loss and capacity decay [26]. Another effect of Jahn–Teller distortion is the irreversible layer-to-spinel transformation. As for the pure layered  $\text{LiMnO}_2$ , this structure transformation starts during the initial delithiation process (the first charge), and can transform into spinel phase completely after several cycles [27,28], and ion-doping is usually involved to prohibit the structure transformation of  $m\text{-LiMnO}_2$  cathode material [4–10]. As for the product R1 and R2, which has a Mn average valance state of +3.75 and +3.57, their charge/discharge profiles still retain a feature of layered structure even in the 20th cycle, and very weak spinel related peaks at  $\sim 4.0$  V can be observed in their  $dQ/dV$  plots as shown in Fig. 5b. In contrast, the charge/discharge profiles of the 20th cycle for R3 and R4 contain two plateaus at  $\sim 4.0$  and  $\sim 2.8$  V, which can be ascribed to  $\text{Li}^+$  inserting into empty 8a tetrahedral sites and 16c octahedral sites of spinel structure [29], respectively. Moreover, it is a pity that all composites transformed into spinel type in the 50th cycle as showing in Fig. 5a and b. The above evolution of charge/discharge profiles suggests that  $\text{Li}_2\text{MnO}_3$  can restrict the irreversible layer-to-spinel transformation and the structure transformation rate is related to the  $\text{Li}_2\text{MnO}_3$  content in the composites. Generally speaking, more than 50%  $\text{Li}_2\text{MnO}_3$  in the composite can effectively slow down the transformation process (especially in the initial several cycles), and too much  $\text{Li}_2\text{MnO}_3$  usually resulted in low reversible capacity. Therefore, the product R1 and R2 have better cyclic performance but with a lower discharge capacity as compared to the product R3 and R4, and the product with a composition of  $0.57\text{Li}_2\text{MnO}_3 \cdot 0.43\text{LiMnO}_2$  has enough  $\text{Li}_2\text{MnO}_3$  to stabilize the structure of  $\text{LiMnO}_2$ , and resulting in the best cyclic performance with a high reversible capacity among those composites.

The discharge capacities of these samples at a current density from 30 to 1200 mA g<sup>-1</sup> under 25 °C and a 4.8 V cut-off voltage are plotted in Fig. 6a. As can be seen, all  $x\text{Li}_2\text{MnO}_3 \cdot (1-x)\text{LiMnO}_2$  composites have much higher discharge capacity than the pristine

$\text{Li}_2\text{MnO}_3$ , and the product R2 with  $x = 0.57$  has the highest discharge capacity at a current density  $>100$  mA g<sup>-1</sup>, and a discharge capacity of 67 mAh g<sup>-1</sup> is still maintained even at 1200 mA g<sup>-1</sup>. However, the discharge capacity is increasing along with descending the  $x$  value under a 4.4 V cut-off voltage as can be seen from Fig. 6b, which is entirely different from the above situation under a 4.8 V cut-off voltage. Furthermore, when charged to 4.8 V in the first cycle and then cycled between 2.0 and 4.4 V, the rate performance of those samples (Fig. 6c) has a changing trend similar to that at 4.4 V cut-off voltage (Fig. 6b), and the capacities of R1, R2, R3 and R4 at high current density (1.2 A g<sup>-1</sup>) are nearly equal to each other, which is similar to that at 4.8 V cut-off voltage as shown in Fig. 6a. Nevertheless, all composites have much higher discharge capacities than the pristine  $\text{Li}_2\text{MnO}_3$  at different current densities under both 4.4 and 4.8 V cut-off voltage. The above different rate performances and changing trends under different cut-off voltages can be ascribed to different activation degrees of the components in the composite, structure transformation, charge transfer in composites, which will further discussed in the following sections.

Usually, the rate performance at a 4.8 V cut-off voltage is associated with the charge transfer and  $\text{Li}^+$  diffusion in electrodes, and its information can be observed from the EIS spectra of the corresponding cells at an open-circuit voltage. The Nyquist plots of these samples after three charge/discharge cycles are shown in Fig. 7a and b, and the corresponding fitting results according to the equivalent circuit inserted in Fig. 7c are listed in Table 2. Among those parameters,  $R_s$  is the main ohmic resistance of the electrolyte and the current collector, and  $R_i$  is the resistance of surface film and  $C_i$  is a constant phase elements (CPE) related to the surface film capacitance.  $R_i$  and  $C_i$  is associated to the semicircle among high frequency range in the Nyquist plots. The value of  $R_i$  is much bigger than  $R_s$  and changes slightly.  $R_e$  and constant phase element ( $C_e$ ) represent the electronic resistance of the cathode material and the associated capacitance [30].  $R_e$  and  $C_e$  is related to the semicircle among

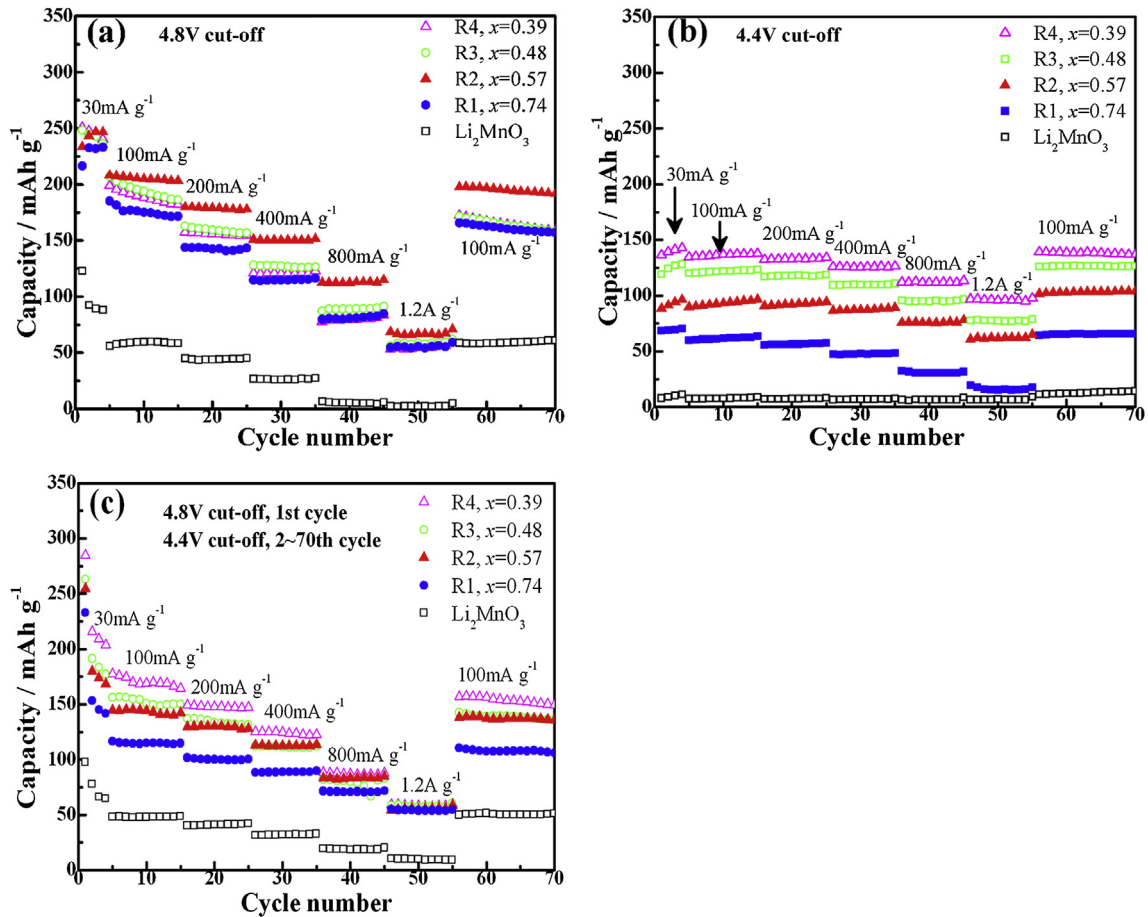


**Fig. 6.** Rate performance of  $\text{Li}_2\text{MnO}_3$  and  $x\text{Li}_2\text{MnO}_3 \cdot (1-x)\text{LiMnO}_2$  ( $x = 0.39, 0.48, 0.57, 0.74$ ) under different cut-off voltages: (a) 4.8 V, (b) 4.4 V, and (c) 4.8 V in the first cycle and then 4.4 V in the following cycles.

middle-to-high frequency range. At high temperature (for example, 25 °C), the two semicircles related to  $R_i$ ,  $C_i$ ,  $R_e$  and  $C_e$  are always merged into one compressed semicircle, but at low temperature (for example, 10 °C), the two semicircle begin to separate from each other [30].  $R_{ct}$  stands for the charge transfer resistance between the active material and electrolyte and  $C_{dl}$  is a CPE related to double layer capacitance.  $R_{ct}$  and  $C_{dl}$  result in a semicircle from medium to low frequency range.  $Z_W$  represents the Warburg impedance related to the straight slope among low frequency range and it is associated to the Li ion diffusion in the active material of cathode [30–32]. To examine whether this equivalent circuit is suitable for fitting these EIS spectra or not, the raw data and fitting results of the EIS spectra of Li/R4 cells cycled under different cut-off voltages are typically plotted together. As shown in Fig. 7d, the raw data and fitting results are overlapped, indicating that these data can be well fitted by the equivalent circuit shown in Fig. 7c.

As can be seen from the Nyquist plots of all samples cycled under 4.8 V cut-off voltage (Fig. 7a), the two semicircles related to  $R_i/C_i$  and  $R_e/C_e$  are combined into a semicircle-like arc from high to medium frequency. The  $R_{ct}/C_{dl}$  related semicircle and the  $Z_W$  related straight slope are undistinguishable and combined into an arc in the low frequency range. In three electrode system, the surface resistance related  $R_i$  and charge transfer resistance related  $R_{ct}$  are attributed to the surface properties of cathode. Passive SEI layer is formed due to the oxidation of electrolyte, which is accompanied with the formation of  $\text{Li}_2\text{CO}_3$  during the electrochemical activation of  $\text{Li}_2\text{MnO}_3$  component in Li-rich solid solution materials [24,33]. The above SEI layer and  $\text{Li}_2\text{CO}_3$  can obstruct the charge transfer

(especially the electron). Besides, the lattice rearrangement process during cycling can lead to a disordered surface structure for the active material particles in cathode [34], which is also obstruct the charge transfer, especially for  $\text{Li}^+$ . The surface condition of cathode is so complicated that the changes of  $R_i$  and  $R_{ct}$  are not linear with the  $\text{Li}_2\text{MnO}_3$  content in those composites as shown in Table 2. As for the pristine  $\text{Li}_2\text{MnO}_3$ , since too much electrolyte is decomposed and too much  $\text{Li}_2\text{CO}_3$  is formed during the electrochemical activation, which results in the largest  $R_i$  and  $R_{ct}$  among these samples. R1 and R2 have some carbon residue and contain relatively low  $\text{Li}_2\text{MnO}_3$  content, so their  $R_i$  and  $R_{ct}$  are smaller than that of the pristine  $\text{Li}_2\text{MnO}_3$ . The  $\text{Li}_2\text{MnO}_3$  contents in R3 and R4 are lower than that in R1 and R2, but it is too low to stabilize the structure, which leads to more lattice rearrangement on the active material surface and more Mn dissolution [34,35]. As a result, although R3 and R4 have less  $\text{Li}_2\text{MnO}_3$  to activate and more carbon residues, their  $R_i$  and  $R_{ct}$  are larger than that of R2. Namely, R2 has the smallest  $R_i$  and  $R_{ct}$  values among these composites as shown in Table 2, and therefore exhibits the best rate performance at 4.8 V cut-off voltage.  $R_e$  decreases dramatically with the decreasing of  $\text{Li}_2\text{MnO}_3$  content but increases slightly when the  $\text{Li}_2\text{MnO}_3$  content is lower than 0.48. In Mn based cathode materials, such as spinel  $\text{Li}_{1-x}\text{Mn}_2\text{O}_4$ , the electronic conductivity is contributed by electron hopping between Mn cations with different valence [36,37]. Therefore, the electronic conductivity is governed by the concentration of charge (electron in low valence Mn, such as  $\text{Mn}^{3+}$ ) and the hopping length (Mn–Mn distance). The Mn–O bonds are lengthened as the lowering of Mn valence [38], hence the lengthening of Mn–Mn distance. For these

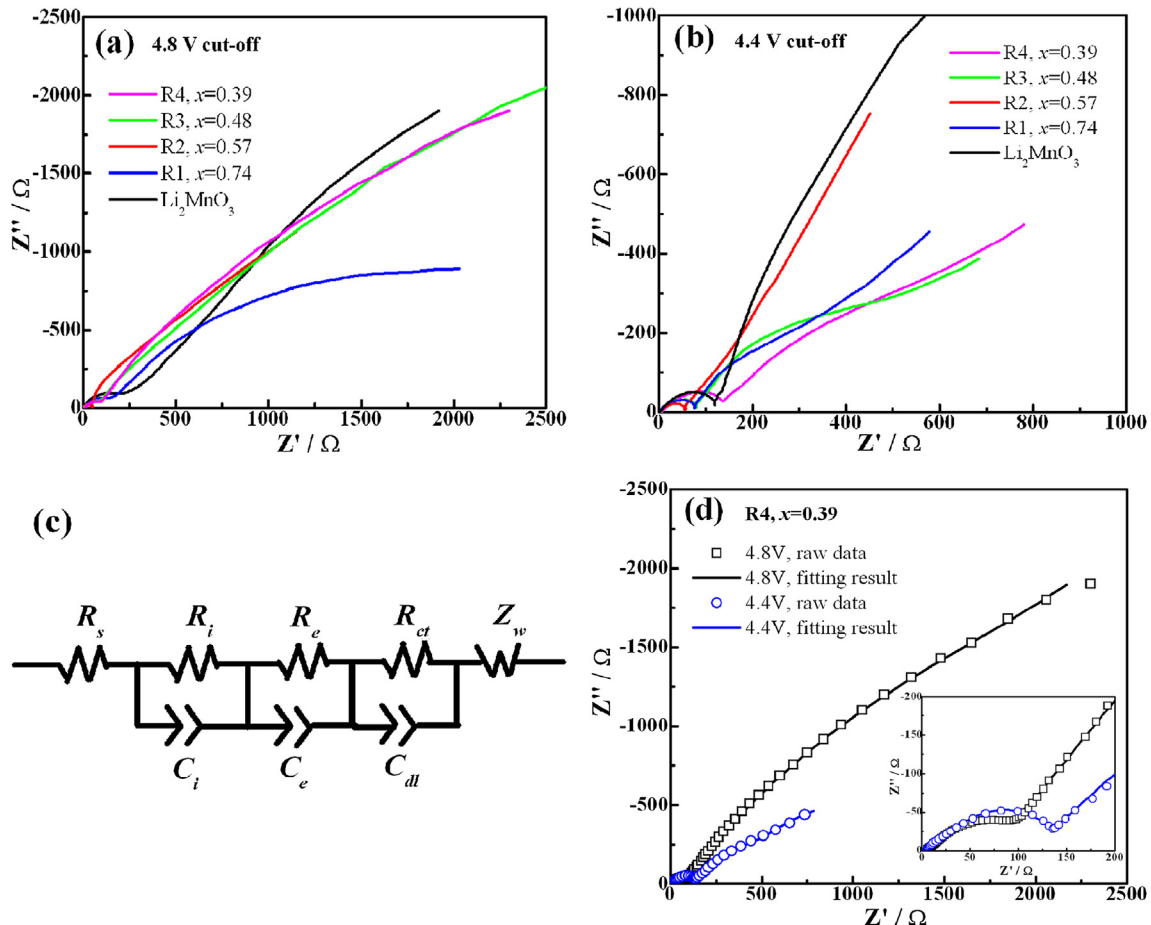


**Fig. 7.** Nyquist plots of  $\text{Li}_2\text{MnO}_3$  and  $x\text{Li}_2\text{MnO}_3 \cdot (1-x)\text{LiMnO}_2$  ( $x = 0.39, 0.48, 0.57, 0.74$ ) cells after 3 charge/discharge cycles under 4.8 V (a) or 4.4 V (b) cut-off voltage; the equivalent circuit proposed for the fitting of these EIS spectra (c); the comparing of fitting results and raw data for the sample R4 (d).

obtained materials discussed above, the valence of Mn decreases as the decreasing of  $\text{Li}_2\text{MnO}_3$  content, therefore the molar ratio of  $\text{Mn}^{3+}$  increases, hence the increasing of charge carriers and electronic conductivity. However, when the valence of Mn is too low, the Mn–Mn distance is too long and the electron hopping is too hard, leading to the decreasing of electronic conductivity and increasing of  $R_e$  [30]. These two opposite effects result in a complicated change of  $R_e$  for these samples cycled under different cut-off voltage.

The EIS spectra of those composite's cells cycled under a 4.4 V cut-off voltage (Fig. 7b) have a similar shape to those tested under

4.8 V cut-off voltage. Table 2 shows a same trend of  $R_s$  and  $R_{ct}$  under different cut-off voltage, but values of  $R_s$  and  $R_{ct}$  under 4.4 V cut-off voltage are smaller than that under 4.8 V cut-off voltage. Since limited  $\text{Li}_2\text{MnO}_3$  is activated under 4.4 V, and the electrolyte decomposition and insulator-like byproducts (such as  $\text{Li}_2\text{CO}_3$ ) formed during the electrochemical activation process are less than that under 4.8 V cut-off voltage, which are beneficial for lowering the resistance of these cells. On the other hand, most  $\text{Li}_2\text{MnO}_3$  in those composites is not electrochemically activated under 4.4 V, the structure defects resulted from the activation of  $\text{Li}_2\text{MnO}_3$  are also limited, which is beneficial for the  $\text{Li}^+$  diffusion, and therefore the capacity retention (the ratio between capacity at  $1.2 \text{ A g}^{-1}$  and  $30 \text{ mA g}^{-1}$ ) under 4.4 V cut-off voltage is much larger than that under 4.8 V cut-off voltage. For example, the capacity retention ratio for R2 is 65% under 4.4 V cut-off voltage, while it is only 27% under 4.8 V cut-off voltage. In addition, the pristine  $\text{Li}_2\text{MnO}_3$  has the poorest rate performance among these samples since it is nearly electrochemically inactive below 4.4 V. Namely, although a high cut-off voltage (4.8 V) can fully activate the present composites to obtain a high reversible capacity, it is detrimental to the structure stability and then to the electrochemical performances. Therefore, a suitable  $\text{Li}_2\text{MnO}_3/\text{LiMnO}_2$  molar ratio in the present composites can alleviate this detriment and the product R2 with  $x = 0.57$  has the optimized molar ratio and crystal structures.

To further validate the above viewpoint, R2 is chosen to perform cyclic voltammogram (CV) tests to obtain the information of redox reaction during the charge/discharge processes. Firstly, a cell is

**Table 2**

The fitting results of EIS spectra of  $\text{Li}_2\text{MnO}_3$  and  $x\text{Li}_2\text{MnO}_3 \cdot (1-x)\text{LiMnO}_2$  cells after 3 charge/discharge cycles.

	$x\text{Li}_2\text{MnO}_3 \cdot (1-x)\text{LiMnO}_2$	$R_s/\Omega$	$R_i/\Omega$	$R_e/\Omega$	$R_{ct}/\Omega$
<i>4.8 V cut-off</i>					
$\text{Li}_2\text{MnO}_3$	$\text{Li}_2\text{MnO}_3$	2.3	35.4	156.1	7159
R1	0.74 $\text{Li}_2\text{MnO}_3 \cdot 0.26\text{LiMnO}_2$	1.7	22.4	108.7	2785
R2	0.57 $\text{Li}_2\text{MnO}_3 \cdot 0.43\text{LiMnO}_2$	1.2	10.6	35.1	557
R3	0.48 $\text{Li}_2\text{MnO}_3 \cdot 0.52\text{LiMnO}_2$	1.2	18.1	44.8	2127
R4	0.39 $\text{Li}_2\text{MnO}_3 \cdot 0.61\text{LiMnO}_2$	1.6	23.3	54.7	4319
<i>4.4 V cut-off</i>					
$\text{Li}_2\text{MnO}_3$	$\text{Li}_2\text{MnO}_3$	1.5	20.4	96.8	772
R1	0.74 $\text{Li}_2\text{MnO}_3 \cdot 0.26\text{LiMnO}_2$	1.2	15.5	58.2	235
R2	0.57 $\text{Li}_2\text{MnO}_3 \cdot 0.43\text{LiMnO}_2$	1.5	6.5	46.0	35
R3	0.48 $\text{Li}_2\text{MnO}_3 \cdot 0.52\text{LiMnO}_2$	1.3	14.1	54.2	304
R4	0.39 $\text{Li}_2\text{MnO}_3 \cdot 0.61\text{LiMnO}_2$	1.2	19.3	98.6	336

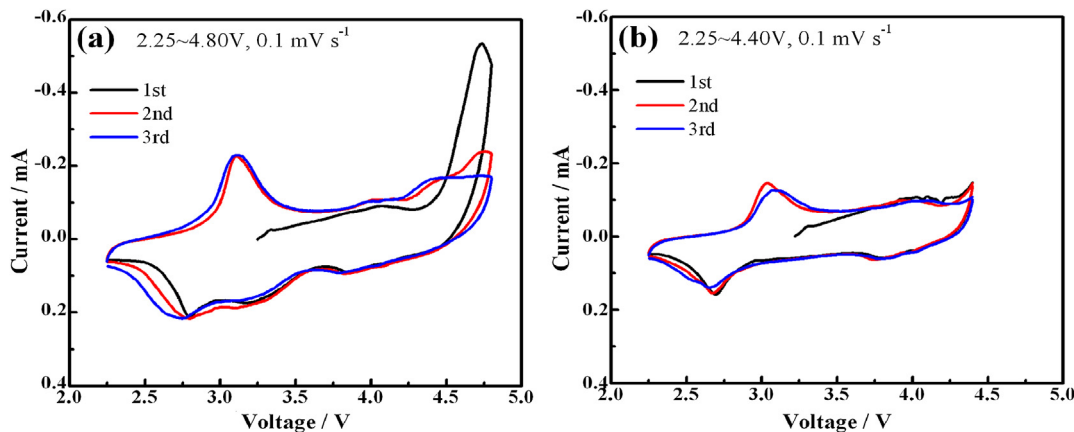


Fig. 8. Cyclic voltammograms of Li/R2 cells under different cut-off voltages.

cycled between 2.25 and 4.80 V (Fig. 8a) or 4.40 V (Fig. 8b) at a scan rate of 0.1 mV s<sup>-1</sup> for 3 cycles from an open-circuit voltage. As shown in Fig. 8a, the anodic peak in the first cycle is at ~4.6 V, which can be ascribed to the activation of Li<sub>2</sub>MnO<sub>3</sub> [15]. The high voltage anodic peak has no symmetric cathodic peak, indicating that this process is not reversible. In the following cycles, a couple peaks symmetrically locate at ~3.0 V and their intensity is stable with cycling. When the test is performed between 2.25 and 4.40 V, the anodic peak at ~4.6 V in the first cycle disappears, but the two symmetry peaks at ~3.0 V are still can be observed in the following cycles, indicating that R2 is electrochemically active below 4.4 V, which is different from the pristine Li<sub>2</sub>MnO<sub>3</sub>. Moreover, the almost overlapped CV curves demonstrate the good reversibility and structure stability of product R2 between 2.25 and 4.40 V. On the other hand, some weak and wide peaks at ~4.0 V, which corresponds to the redox process related to spinel phase, can be observed from both Fig. 8a and b, while they are too weak to be observed from the dQ/dV curves in Fig. 5b. This indicates that the layer-to-spinel transformation still occurs, but be weakened dramatically in R2. In fact, such transformation process is common for the other Li-rich solid solution cathode materials and need further investigation [15,39,40]. Anyway, the above CV results further confirmed that the reaction related Li<sub>2</sub>MnO<sub>3</sub> at ~4.6 V is irreversible, while the redox reaction of R2 during the charge/discharge processes locates at ~3.0 V, which can maintain a good reversible and stable capacity when the cell is charged below 4.4 V.

Based on the above experimental results and discussion, the initial capacity, cyclic and rate performances of  $x$ Li<sub>2</sub>MnO<sub>3</sub>·(1- $x$ )LiMnO<sub>2</sub> are significantly improved as compared to the pristine Li<sub>2</sub>MnO<sub>3</sub>. Although the initial discharge capacity is increasing as enhancing the LiMnO<sub>2</sub> content, its layered structure is becoming unstable, and therefore resulting in 0.57Li<sub>2</sub>MnO<sub>3</sub>·0.43LiMnO<sub>2</sub> showing an optimized electrochemical property. The detailed reason may be that it contains enough Li<sub>2</sub>MnO<sub>3</sub> to stabilize the LiMnO<sub>2</sub> structure and has a suitable Mn average valence to maintain a balance between the reversible capacity and Jahn–Teller distortion. The present results confirmed that the present method may be helpful to improve the electrochemical performances of Li<sub>2</sub>MnO<sub>3</sub> related materials.

#### 4. Conclusions

$x$ Li<sub>2</sub>MnO<sub>3</sub>·(1- $x$ )LiMnO<sub>2</sub> ( $x$  = 0.39, 0.48, 0.57, 0.74) composites with layered structure were successfully synthesized by partially reducing the electrochemically inactive Li<sub>2</sub>MnO<sub>3</sub> at the normal voltage range (<4.4 V vs. Li<sup>+</sup>/Li). As cathode material of Li-ion

battery, this kind of composite materials can present an initial charge/discharge feature similar to the other Li-excess materials. These composites also exhibit a high reversible capacity (>210 mAh g<sup>-1</sup>) and a remarkably enhanced rate performance as compared to the pristine Li<sub>2</sub>MnO<sub>3</sub>. The presence of LiMnO<sub>2</sub> can make these composites electrochemically active under a 4.4 V cut-off voltage and the Li<sub>2</sub>MnO<sub>3</sub> can stabilize the layered structure of LiMnO<sub>2</sub>, and an optimized  $x$  value is 0.57, which leads to a suitable Mn average valence that can maintain a balance between the capacity and Jahn–Teller distortion. Although the cyclic performance is still not satisfactory, the low cost of such Co/Ni-free Mn-based layered Li-rich composites should be a new kind cathode material for the potential commercial use.

#### Acknowledgments

This work was supported by the Program for New Century Excellent Talents in University (NCET-07-0637) of China.

#### References

- [1] N.S. Choi, Z.H. Chen, S.A. Freunberger, X.L. Ji, Y.K. Sun, K. Amine, G. Yushin, L.F. Nazar, J. Cho, P.G. Bruce, *Angew. Chem. Int. Ed.* 51 (2012) 9994–10024.
- [2] J. Molenda, M. Ziernicki, J. Marzec, W. Zajac, M. Molenda, M. Bucko, *J. Power Sources* 173 (2007) 707–711.
- [3] A.R. Armstrong, P.G. Bruce, *Nature* 381 (1996) 499–500.
- [4] S.T. Myung, S. Komaba, N. Hiroasaki, N. Kumagai, *Electrochem. Commun.* 4 (2002) 397–401.
- [5] A.D. Robertson, A.R. Armstrong, A.J. Fowkes, P.G. Bruce, *J. Mater. Chem.* 11 (2001) 113–118.
- [6] T.E. Quine, M.J. Duncan, A.R. Armstrong, A.D. Robertson, P.G. Bruce, *J. Mater. Chem.* 10 (2000) 2838–2841.
- [7] Y.I. Jang, B.Y. Huang, Y.M. Chiang, D.R. Sadoway, *Electrochem. Solid-State Lett.* 1 (1998) 13–16.
- [8] Z. Su, Z.W. Lu, X.P. Gao, P.W. Shen, X.J. Liu, J.Q. Wang, *J. Power Sources* 189 (2009) 411–415.
- [9] T.J. Kim, D. Son, J. Cho, B. Park, *J. Power Sources* 154 (2006) 268–272.
- [10] P. Suresh, A.K. Shukla, N. Munichandraiah, *J. Power Sources* 161 (2006) 1307–1313.
- [11] A. Boulineau, L. Croguennec, C. Delmas, F. Weill, *Chem. Mater.* 21 (2009) 4216–4222.
- [12] M.M. Thackeray, S.H. Kang, C.S. Johnson, J.T. Vaughey, R. Benedek, S.A. Hackney, *J. Mater. Chem.* 17 (2007) 3112–3215.
- [13] C.S. Johnson, J.S. Kim, C. Lefief, N. Li, J.T. Vaughey, M.M. Thackeray, *Electrochem. Commun.* 6 (2004) 1085–1091.
- [14] M.M. Thackeray, S.H. Kang, C.S. Johnson, J.T. Vaughey, S.A. Hackney, *Electrochem. Commun.* 8 (2006) 1531–1538.
- [15] C.S. Johnson, N.C. Li, C. Lefief, J.T. Vaughey, M.M. Thackeray, *Chem. Mater.* 20 (2008) 6095–6106.
- [16] C.S. Johnson, N. Li, J.T. Vaughey, S.A. Hackney, M.M. Thackeray, *Electrochem. Commun.* 7 (2005) 528–536.
- [17] C.S. Johnson, *J. Power Sources* 165 (2007) 559–565.
- [18] Y. Yongli, W. Naizhi, Z. Xiujuan, Z. Xiujing, W. Caimin, *Metall. Anal.* 27 (2007) 20–23.

- [19] Q. Zhang, T. Peng, D. Zhan, X. Hu, G. Zhu, *Mater. Chem. Phys.* 138 (2013) 146–153.
- [20] M.A. Osman, U.W. Suter, *Chem. Mater.* 14 (2002) 4408–4415.
- [21] X. Shi, R. Rosa, A. Lazzari, *Langmuir* 26 (2010) 8474–8482.
- [22] A.D. Robertson, P.G. Bruce, *Chem. Commun.* (2002) 2790–2791.
- [23] S.F. Amalraj, B. Markovsky, D. Sharon, M. Taliander, E. Zinigrad, R. Persky, O. Haik, J. Grinblat, J. Lampert, M. Schulz-Dobrick, A. Garsuch, L. Burlaka, D. Aurbach, *Electrochim. Acta* 78 (2012) 32–39.
- [24] N. Yabuchi, K. Yoshii, S.T. Myung, I. Nakai, S. Komaba, *J. Am. Chem. Soc.* 133 (2011) 4404–4419.
- [25] J. Cho, Y.J. Kim, T.J. Kim, B. Park, *J. Electrochem. Soc.* 149 (2002) A127–A132.
- [26] D.H. Jang, Y.J. Shin, S.M. Oh, *J. Electrochem. Soc.* 143 (1996) 2204–2211.
- [27] Y.I. Jang, B.Y. Huang, H.F. Wang, D.R. Sadoway, Y.M. Chiang, *J. Electrochem. Soc.* 146 (1999) 3217–3223.
- [28] Y. Shao-Horn, S.A. Hackney, A.R. Armstrong, P.G. Bruce, R. Gitzendanner, C.S. Johnson, M.M. Thackeray, *J. Electrochem. Soc.* 146 (1999) 2404–2412.
- [29] T. Ohzuku, M. Kitagawa, T. Hirai, *J. Electrochem. Soc.* 137 (1990) 769–775.
- [30] Q.C. Zhuang, T. Wei, L.L. Du, Y.L. Cui, L. Fang, S.G. Sun, *J. Phys. Chem. C* 114 (2010) 8614–8621.
- [31] S.J. Shi, J.P. Tu, Y.Y. Tang, Y.Q. Zhang, X.Y. Liu, X.L. Wang, C.D. Gu, *J. Power Sources* 225 (2013) 338–346.
- [32] M.D. Levi, G. Salitra, B. Markovsky, H. Teller, D. Aurbach, U. Heider, L. Heider, *J. Electrochem. Soc.* 146 (1999) 1279–1289.
- [33] Y. Matsuo, R. Kostecki, F. McLarnon, *J. Electrochem. Soc.* 148 (2001) A687–A692.
- [34] J. Vetter, P. Novak, M.R. Wagner, C. Veit, K.C. Moller, J.O. Besenhard, M. Winter, M. Wohlfahrt-Mehrens, C. Vogler, A. Hammouche, *J. Power Sources* 147 (2005) 269–281.
- [35] Z. Li, F. Du, X.F. Bie, D. Zhang, Y.M. Cai, X.R. Cui, C.Z. Wang, G. Chen, Y.J. Wei, *J. Phys. Chem. C* 114 (2010) 22751–22757.
- [36] G. Pistoia, D. Zane, Y. Zhang, *J. Electrochem. Soc.* 142 (1995) 2551–2557.
- [37] J. Marzec, K. Swierczek, J. Przewoznik, J. Molenda, D.R. Simon, E.M. Kelder, J. Schoonman, *Solid State Ionics* 146 (2002) 225–237.
- [38] D. Pasero, V. McLaren, S. de Souza, A.R. West, *Chem. Mater.* 17 (2005) 345–348.
- [39] J. Hong, D.H. Seo, S.W. Kim, H. Gwon, S.T. Oh, K. Kang, *J. Mater. Chem.* 20 (2010) 10179–10186.
- [40] A. Boulineau, L. Simonin, J.F. Colin, E. Canevet, L. Daniel, S. Patoux, *Chem. Mater.* 24 (2012) 3558–3566.